# Pattern-induced local symmetry breaking in active matter systems

**Jonas Denk**[a,b,c] **and Erwin Frey**[a,*]

[a]Arnold Sommerfeld Center for Theoretical Physics (ASC) and Center for NanoScience (CeNS), Department of Physics, Ludwig-Maximilians-Universität München, Theresienstrasse 37, D-80333 München, Germany
[b]Department of Physics, University of California, Berkeley, CA 94720, USA
[c]Department of Integrative Biology, University of California, Berkeley, CA 94720, USA

**The emergence of macroscopic order and patterns is a central paradigm in systems of (self-)propelled agents, and a key component in the structuring of many biological systems. The relationships between the ordering process and the underlying microscopic interactions have been extensively explored both experimentally and theoretically. While emerging patterns often show one specific symmetry (e.g. nematic lane patterns or polarized traveling flocks), depending on the symmetry of the alignment interactions patterns with different symmetries can apparently coexist. Indeed, recent experiments with an actomyosin motility assay suggest that polar and nematic patterns of actin filaments can interact and dynamically transform into each other. However, theoretical understanding of the mechanism responsible remains elusive. Here, we present a kinetic approach complemented by a hydrodynamic theory for agents with mixed alignment symmetries, which captures the experimentally observed phenomenology and provides a theoretical explanation for the coexistence and interaction of patterns with different symmetries. We show that local, pattern-induced symmetry breaking can account for dynamically coexisting patterns with different symmetries. Specifically, in a regime with moderate densities and a weak polar bias in the alignment interaction, nematic bands show a local symmetry-breaking instability within their high-density core region, which induces the formation of polar waves along the bands. These instabilities eventually result in a self-organized system of nematic bands and polar waves that dynamically transform into each other. Our study reveals a mutual feedback mechanism between pattern formation and local symmetry breaking in active matter that has interesting consequences for structure formation in biological systems.**

active matter theory | pattern formation | emergent symmetries | pattern coexistence

**Correspondence:** *frey@lmu.de*

Any theory for systems of (self-)propelled agents must be based on assumptions regarding the agents' propulsion mechanism as well as their interactions. One of the central insights in active matter theories is that interactions that align the agents' orientations—even if they are short-ranged—can lead to the formation of macroscopic order already in dilute systems in two dimensions (1–4). Close to the onset of macroscopic order, both experiments with (self-)propelled agents and theoretical studies quite generally observe phase separation into high-density ordered clusters and a low-density disordered background, rather than spatially uniform long-range order (3–5). Hence, symmetry breaking in active matter systems seems to be inextricably linked to formation of patterns. In theoretical approaches, the symmetry of the macroscopic

order and the corresponding patterns is typically dictated a priori by the assumed microscopic symmetry of the specific active matter model under consideration (4) [Fig.1(A)]: models with polar interaction symmetry exhibit polar waves (6–10), while models with nematic interaction symmetry show bands (lanes) within which the agents are (preferentially) oriented in parallel (11–13). Thus, in all of these theoretical models, the choice of the underlying microscopic interaction symmetry largely determines the model's phenomenology. This should be seen in light of the observation that in nature or in the laboratory microscopic details of the agent's propulsion mechanism and interactions are often unclear or essentially inaccessible. Moreover, these properties of the agents might not even be inherent features (traits) characterized by a fixed set of parameters, but could in principle dynamically depend on the emergent collective behavior of the agents, as suggested for animal herds (14) or chemical active systems (15, 16).

Recently, experimental studies of actomyosin motility assays reported coexistence of polar and nematic patterns, with actin filaments dynamically cycling between polar waves and nematic band patterns (17). Supported by large-scale computer simulations—emulating the microscopic features of the observed collision statistics—these authors concluded that in this particular case the symmetry of the self-organized patterns is not determined *a priori* by the symmetry of the pairwise interaction between particles, but is itself an *emergent phenomenon* of the many-body system (17). What then is the mechanism underlying this startling phenomenon?

Agent-based simulations indicate that both nematic and polar-ordered clusters can arise when the microscopic alignment between agents is predominantly nematic with a polar contribution, either due to the interactions between extended rods (5, 18, 19) or memory in the orientational noise (20). Furthermore, the existence of distinct regimes of either nematic or polar patterns has been observed in theoretical studies with explicitly mixed alignment symmetries (21–23). However, cycling and transformations between patterns of different symmetries as observed in Ref. (17) were not reported and the theoretical mechanism behind this coexistence is poorly understood (4, 17, 24). Specifically, neither kinetic nor continuum hydrodynamic approaches have so far been able to reproduce or elucidate this phenomenology (4, 24).

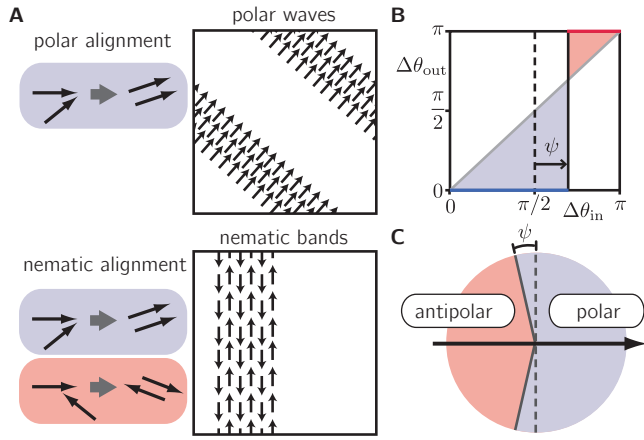While theoretical approaches with mixed microscopic alignment symmetries have considered alignments that depend

**Fig. 1. Symmetries in active matter. (A)** In models with fully polar alignment, polar agents assume the same propulsion direction upon alignment. For fully nematic alignment, particles assume the same or opposing propulsion directions, depending on whether they collide at an acute or obtuse angle, respectively. Polar (nematic) alignment interactions enable macroscopic polar (nematic) order. Beyond the onset of order, the system evolves into wave patterns or nematic bands depending on the symmetry of the alignment interaction. **(B)** 'Collision statistics' for the binary collision rule with polar bias $\psi$. $\Delta\theta_{\text{out}}$ denotes the angle differences between pairwise particle velocities after the collision and is either $0$ or $\pi$ depending on whether the agents' angle difference before the collision, $\Delta\theta_{\text{in}}$, is smaller or larger than $\pi/2 + \psi$, respectively. **(C)** Illustration of our generalized collision assumption. The black arrow indicates the pre-collision orientation of a reference polar agent. Alignment with a second agent is polar if the propulsion of the second particle lies in the blue shaded angular range and antipolar in the red shaded angular range.

on inter-particle distance (21), chance (22) or particle species (23), the computational analysis in Ref. (17) suggested that the emergence of dynamic coexistence critically depends on the simultaneous presence of polar and nematic contributions in the binary collision statistics. Here, motivated by the results in Ref. (17), we propose a kinetic theory for a dilute system of propelled particles with tunable 'binary collision statistics' [Fig.1(B)]. Specifically, we employ a kinetic Boltzmann approach (25) where particles undergo binary collisions that lead to nematic alignment with a small (tunable) polar bias [Fig. 1(C)].

For both vanishing and fully polar bias, our model recovers the well-studied scenarios of purely nematic (13) and purely polar (9, 10) interaction symmetry, respectively. Interestingly, for an intermediate polar bias, our model features a transition from macroscopic nematic order at intermediate densities to macroscopic polar order at high densities. In a regime characterized by intermediate polar bias and intermediate densities, we observe that patterns of polar and nematic symmetry coexist and are dynamically interconvertible, which is reminiscent of the observations in Ref. (17). Based on a combination of stability analyses and numerical simulations we argue that such coexistence depends on the inextricable link between symmetry breaking and pattern formation. For instance, while the system forms nematic bands in a density regime that leads to symmetry breaking towards macroscopic nematic order, the density at the core of these bands increases and eventually exceeds the threshold value for a transition from macroscopic nematic to macroscopic polar order. This spatially local crossing of a critical value in the particle density—a control parameter—triggers local

symmetry breaking, which induces the self-organized formation of polar waves.

To substantiate this hypothetical mechanism as a general mechanism for the coexistence of polar and nematic patterns in active-matter systems, we study simplified hydrodynamic equations which capture pattern formation in a nematic phase as well as a transition from macroscopic nematic to polar symmetry for high densities. Indeed, like our kinetic Boltzmann approach, our hydrodynamic theory exhibits a regime of coexisting polar wave and nematic band patterns.

Our study thus reveals an interesting *mutual feedback* between pattern formation and macroscopic symmetry breaking in active matter. This feedback occurs because the particle density, which shows pattern formation in active systems, is at the same time a control (bifurcation) parameter for the macroscopic symmetry of the system. This twofold role of the particle density transforms symmetry breaking in active systems from a ordering phenomenon under the control of a global parameter into a self-organisation phenomenon with a local interplay between pattern formation and symmetry breaking. We would argue that this interplay represents a fairly general mechanism that allows macroscopic symmetries to be an emergent property in themselves, rather than being imposed directly by microscopic interaction rules.

## Results

**Kinetic Boltzmann approach with polar and nematic contributions.** Our starting point for a mesoscopic theory of aligning agents is the kinetic Boltzmann equation (25). It describes the temporal evolution of the one-particle distribution function $f(\mathbf{r}, \theta, t)$ for the position $\mathbf{r} \in \mathcal{R}^2$ and the orientation $\theta \in [0, 2\pi)$ of self-propelled particles that undergo binary aligning collisions in a dilute (dry) system (25). It reads

$$\partial_t f(\mathbf{r}, \theta, t) + v_0 \, \mathbf{e}_\theta \cdot \partial_\mathbf{r} f(\mathbf{r}, \theta, t) = \mathcal{I}_{\text{diff}}[f] + \mathcal{I}_{\text{coll}}[f, f], \quad \textbf{(1)}$$

where $v_0$ denotes the constant speed of the active particles, $\mathbf{e}_\theta$ is a unit vector pointing along direction $\theta$, and the terms $\mathcal{I}_{\text{diff}}[f]$ and $\mathcal{I}_{\text{coll}}[f, f]$ describe diffusion of individual particles and collisions between particles, respectively (see *SI Appendix*, Note 1). In more detail, spherical particles (with diameter $d$) are assumed to move ballistically with constant speed $v_0$ along their orientations $\theta$ and can change their orientation by diffusion as well as by local binary collision. Diffusion is modeled by a shift in a particle's orientation from $\theta$ to $\theta + \eta$ at a rate $\lambda$, where we assume $\eta$ to be a Gaussian-distributed random variable with standard deviation $\sigma$. Binary collisions between particles are emulated through 'alignment rules' [Fig. 1(B,C)], with an additive random contribution also drawn from a Gaussian distribution with a standard deviation $\sigma'$; in the following we set $\sigma' = \sigma$ for simplicity. In the context of the kinetic Boltzmann approach, a fully nematic interaction rule dictates that particles that collide at an acute angle adopt their average orientation (polar alignment), while particles colliding at an obtuse angle also align, but with opposite orientations (anti-polar alignment). For fully polar alignment, particles adopt their

average orientation irrespective of their pre-collision angle [Fig. 1].

The dynamics of orientational order in the kinetic Boltzmann approach is most conveniently studied by exploiting the fact that the polar vector **P** and nematic tensor **Q** can be expressed in terms of the Fourier modes $f_k(\mathbf{r}, t) = \int_{-\pi}^{\pi} d\theta\, e^{i\theta k} f(\mathbf{r}, \theta, t)$ of the one-particle distribution function:

$$\rho\mathbf{P} = \left( \begin{array}{c} \mathrm{Re}[f_1] \\ \mathrm{Im}[f_1] \end{array} \right), \quad \rho\mathbf{Q} = \frac{1}{2} \left( \begin{array}{cc} \mathrm{Re}[f_2] & \mathrm{Im}[f_2] \\ \mathrm{Im}[f_2] & -\mathrm{Re}[f_2] \end{array} \right). \tag{2}$$

Furthermore, the local particle density $\rho(\mathbf{r}, t)$ is given by the $k=0$ mode: $\rho(\mathbf{r}, t) = f_0(\mathbf{r}, t)$. The dynamics of $f_k(\mathbf{r}, t)$ reads

$$\partial_t f_k + \frac{v_0}{2} \left[ \partial_x(f_{k+1} + f_{k-1}) - i\partial_y(f_{k+1} - f_{k-1}) \right]$$
$$= -\lambda\left(1 - e^{-\frac{1}{2}k\sigma^2}\right)f_k + \sum_{n=-\infty}^{\infty} \mathcal{I}_{n,k} f_n f_{k-n}. \tag{3}$$

Explicit expressions for the collision coefficients $\mathcal{I}_{n,k}$ can be found in *SI Appendix*, Note 1. For $k=0$, Eq. (3) yields the continuity equation $\partial_t \rho(\mathbf{r}, t) = -v_0 \nabla \cdot (\rho\mathbf{P})$.

Solutions of Eq. (3) for fully polar (9, 10) or fully nematic (13) alignment rules, show a transition from disorder, i.e. vanishing polar and nematic order, to nonzero polar or nematic order, respectively, for sufficiently high densities or low noise level $\sigma$. Close to the onset of order, it predicts the formation of patterns, consistent with experimental observations and numerical simulations (3, 19). The kinetic Boltzmann equation thus serves as a useful basis for a qualitative study of the phenomenology of dilute systems of self-propelled particles.

Recent experimental results from the actin motility assay and corresponding simulation results from agent-based models (17) strongly suggest that the relative weights of polar and nematic contributions to the binary collision statistics are critical for the self-organization of spatio-temporal patterns. As a minimal extension of fully polar or nematic alignment rules (25), we propose a collision rule with a small tunable polar bias. Specifically, we assume that colliding particles align in a polar manner when their velocities form an angle difference smaller than $\frac{\pi}{2} + \psi$ with $\psi \in [0, \frac{\pi}{2}]$ and align anti-polar otherwise [Fig. 1(B,C)]. The parameter $\psi$ thus characterizes the polar bias, where for $\psi = 0$ and $\psi = \frac{\pi}{2}$ the collision rule reduces to fully nematic and fully polar collisions, respectively. It is convenient to rescale time, space, and density such that $v_0 = \lambda = d = 1$. Then, the only remaining free parameters are the noise amplitude $\sigma$, the polar bias $\psi$, and the mean particle density $\bar{\rho} = \frac{1}{A} \int_A d\mathbf{r} \int_{-\pi}^{\pi} d\theta\, f(\mathbf{r}, \theta, t)$ measured in units of $\lambda/(dv_0)$, i.e. the number of particles found within the area traversed by a particle between successive diffusion events.

**Phase diagram and a nonlinear transition to polar order.** Since the collision coefficients $\mathcal{I}_{n,k}$ are zero for $k=0$, Eq. (3) possesses a spatially uniform solution with zero order, i.e. $f_k = 0$ for $|k| > 0$, and uniform density $f_0 = \bar{\rho}$. Up
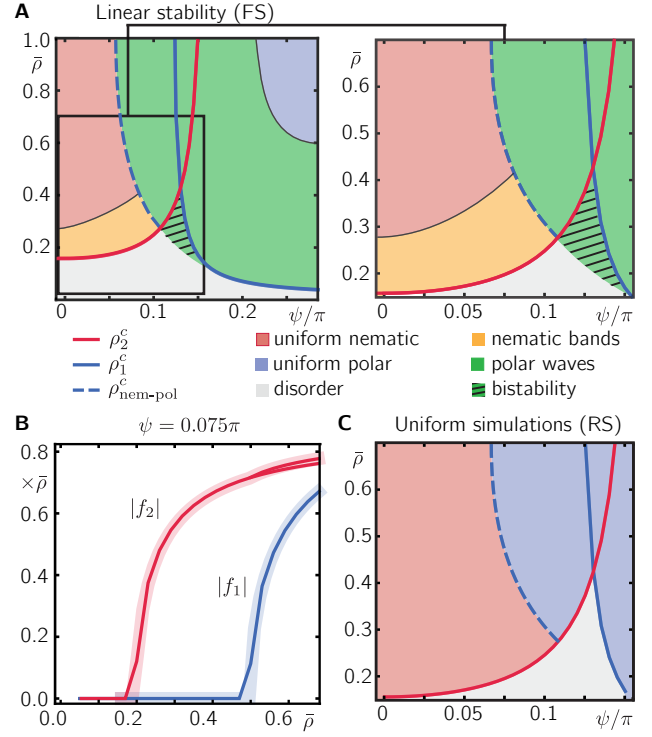


**Fig. 2. Uniform solutions and linear stability. (A)** Regimes and linear stability of spatially uniform solutions for Eq. (3) in angular Fourier space (FS) with a truncation at $k_c = 10$. Squares denote stable solutions, triangles indicate solutions that are unstable against spatial perturbations, suggesting pattern formation. Solid lines denote the critical transition densities $\rho_2^c$ and $\rho_1^c$ from a disordered solution to nematic and polar order, respectively. Our analysis reveals another transition from nematic order to polar order at intermediate polar bias (blue dashed line serves as guide to the eye). **(B)** Spatially uniform solutions for $f_1$ and $f_2$ at $\psi = 0.075\pi$ calculated from the truncated Boltzmann equation in angular Fourier space (solid lines) as compared to spatially uniform solutions of the Boltzmann equation in real space (RS, Eq. (1), shaded lines) calculated using the generalized SNAKE algorithm. **(C)** Phase portrait of spatially uniform solutions using the generalized SNAKE algorithm. Simulations were done on a single lattice point starting at a disordered state with small fluctuations in the angular distribution. The noise value was fixed to $\sigma = 0.2$.

to linear order, a small perturbation $\delta f_k$ of this disordered state evolves according to $\partial_t \delta f_k(t) = \mu_k(\bar{\rho}, \sigma, \psi)\, \delta f_k$ with the growth rate $\mu_k(\bar{\rho}, \sigma, \psi) = (\mathcal{I}_{0,k} + \mathcal{I}_{k,k})\bar{\rho} - \lambda(1 - e^{-\frac{1}{2}k\sigma^2})$. The zeros of these growth rates, $\mu_k(\rho_k^c, \sigma, \psi) = 0$, mark the critical densities $\rho_k^c(\sigma, \psi)$ above which the mode $k$ grows exponentially. While previous studies have focused on the onset of order for fully polar and nematic interactions as a function of the density $\bar{\rho}$ and noise amplitude $\sigma$ (25), in the following we keep the noise level constant, $\sigma = 0.2$, and focus on the onset of order as a function of the polar bias $\psi$. Figure 2(A) shows the critical densities $\rho_1^c(\psi)$ and $\rho_2^c(\psi)$ for the onset of polar and nematic order, respectively. For small and large polar bias, only the growth rate for $k=2$ or $k=1$, respectively, changes sign, indicating that there are transitions from a disordered state to a state with either nematic order (for small polar bias $\psi$) or polar order (for large polar bias $\psi$). In contrast, for intermediate polar bias, the transition densities $\rho_1^c(\psi)$ and $\rho_2^c(\psi)$ cross, implying that there is a regime in the $(\bar{\rho}, \psi)$ phase diagram where the disordered state is linearly unstable under both polar and nematic perturbations.

After identifying the parameter regimes where the spatially uniform disordered solutions become unstable, we now

determine the stable, spatially uniform, ordered solutions of Eq. (3) in these regimes. As this is no longer feasible analytically (due to the infinite sum), we resort to approximate solutions, exploiting the fact that even above the ordering transition, modes with sufficiently large $|k|$ are still negligible (10, 26). To this end, following Ref. (26), we set all spatial derivatives and all Fourier modes $f_k$ beyond a certain cutoff $k_c$ in Eq. (3) to zero, and numerically solve the ensuing equations for all remaining modes with $|k| \leq k_c$. We then performed a linear stability analysis of the resulting spatially uniform solutions against uniform as well as nonuniform (wave-like) perturbations. The directions of spatial perturbations were varied to probe for instabilities perpendicular and parallel to the orientation of the spatially uniform (polar and nematic) order parameters. Based on this analysis we identified the type of order exhibited by spatially uniform solutions, as well as their stability against wave-like perturbation for different values of the average density $\bar{\rho}$ and polar bias $\psi$ [see Fig. 2(A)].

Above the critical transition densities $\rho_2^c(\psi)$ and $\rho_1^c(\psi)$, we indeed find spatially uniform solutions with nonzero nematic and polar order, respectively, as suggested by the linear stability analysis of the disordered state. In addition, within these regimes, we identify subregimes in which the respective spatially uniform solutions are unstable under spatial perturbations, suggesting the formation of spatially *nonuniform* patterns [indicated by the triangles in Fig. 2(A)]. We find that slightly above the transition density to nematic order, $\rho_2^c$, spatially uniform nematic order is unstable against wave-like perturbations perpendicular to the nematic order, which suggests formation of *nematic band patterns*. Furthermore, in a subregime of polar order, uniform polar order is unstable against spatial perturbations parallel to the orientation of polar order, which suggests the emergence of travelling *polar waves*. The prediction of nematic bands and polar waves for small and large polar bias is in accordance with previous studies on systems with either fully nematic or polar interaction symmetries, respectively (25). Interestingly, for sufficiently large polar bias ($\psi \gtrsim 0.05\pi$) and high enough densities ($\bar{\rho} > \rho_2^c$) we identify a transition that has not been observed in previous studies with fully nematic or polar alignment: as the density is increased above $\rho_{nem-pol}^c(\psi)$ [indicated by the dashed line in Fig. 2(A)], there is a direct transition from solutions with uniform nematic order to solutions with uniform polar order. Furthermore, within the regime of linearly stable disorder, and close to the intersection of $\rho_1^c$ and $\rho_2^c$, our analysis reveals a regime of *bistability*. Here, we find both linearly stable disorder and uniform polar order, which is linearly unstable to polar wave patterns. This bistability of disorder and polar patterns is an interesting topic in its own right and is in fact closely related to the observation of a discontinuous transition between the isotropic and the ordered phase in the homogeneous regime as indicated for aligning hard discs (27, 28). We will defer the study of this bistability regime to future work and focus here on the transition from nematic to polar order.

To independently test the predictions of our approximate so-

lutions and linear stability analyses, we numerically solved the Boltzmann equation, Eq. (1), in real space (for details see *SI Appendix*, Note 2). To this end, we used a modified version of the SNAKE algorithm (29). To determine the uniform solutions, we simulated a spatially uniform system [see Fig. 2(C)] and find excellent agreement with the approximate solutions of our spectral analysis [Fig. 2(B), compare (A) with (C)].

**Pattern formation leads to dynamic transformations between nematic and polar symmetries.** To resolve the spatio-temporal dynamics of the kinetic Boltzmann equation, Eq. (1), especially in regimes where our stability analysis predicts spatially uniform solutions to be unstable, we employed our modified SNAKE algorithm for a spatially extended system to numerically solve the Boltzmann equation Eq. (1) in extensive parameter sweeps in both the global density and polar bias. [Fig. 3(A)] shows simulation results (symbols) against the background of our predictions from linear stability analysis (shaded) [Fig. 2(A)].

For vanishing and small polar bias, our numerical simulations show nematic band solutions for densities slightly above $\rho_2^c(\psi)$ and uniform nematic states at higher densities [orange and red symbols in Fig. 3(A), respectively; see *SI Appendix*, Note 2, Fig.S1(A)]. For larger polar bias, we find regimes of traveling-wave solutions and spatially uniform polar-ordered states consistent with our predictions from linear stability analysis [green and blue symbols in Fig. 3(A), respectively; see *SI Appendix*, Note 2, Fig.S1(B)]. The regimes of patterns and uniformly ordered solutions are in good agreement with
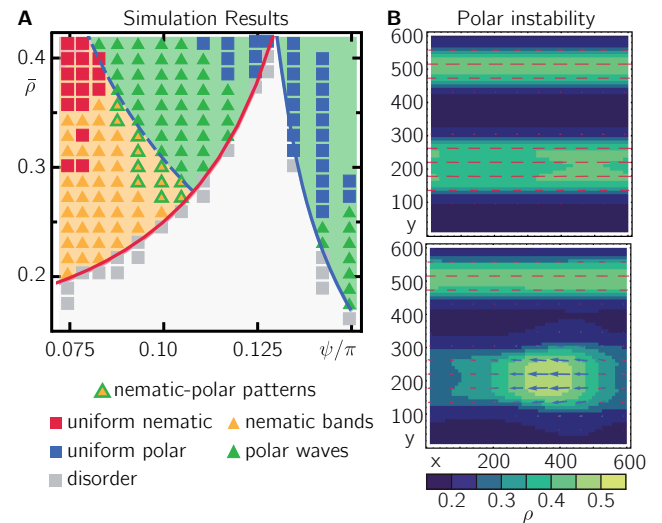


**Fig. 3. Dynamic transformations between nematic and polar patterns. (A)** Numerical solutions of Eq. (1) display regimes of uniform nematic and polar order as well as nematic band and traveling wave patterns (symbols as in Fig. 2(A)). The green and orange shades denote regimes in which linear stability analysis predicts polar and nematic patterns, respectively (regimes in Fig. 2(A,C)). In addition to the states predicted by linear stability analysis (Fig. 2), we find dynamic transformations between patterns of nematic to polar patterns below $\rho_{nem-pol}^c$. **(B)** Simulation snapshots in the regime of dynamic transformations (nematic-polar patterns) shortly before (top) and after (bottom) a local instability within the core of a nematic band. Red bars and blue arrows indicate the orientation and strength of local nematic and polar order, respectively. All simulations started from uniform disordered states with small random fluctuations. For details on the simulations see *SI Appendix*, Note 2.

our linear stability analysis [Fig. 2(A)].

Remarkably, we find patterns with polar order even for densities below $\rho^c_{\text{nem-pol}}$ [nematic-polar patterns in Fig. 3(A)]. Here, the spatio-temporal dynamics of the system exhibits both patterns with polar and nematic order that dynamically interconvert into each other [Fig. 3(B); see *SI Appendix*, Note 2, Movie 1-3]. Starting from a disordered state, the nematic order grows quickly and the system starts to exhibit high-density nematic band patterns (in line with linear stability analysis). While the ensuing average nematic order is approximately the same as that found for spatially uniform solutions of Eq. (3), the local nematic order is much higher *within* the nematic bands and approaches zero in the disordered regions between the bands (see *SI Appendix*, Note 2, Fig.S2). Actually, the local density in the center of a band is so high that it by far exceeds the density at the onset of the nematic-polar order transition $\rho^c_{\text{nem-pol}}$. This suggests that within a band, purely nematic order eventually becomes unstable and polar order starts to emerge there. Indeed, we observe that after some time, polar order locally builds up in the nematic bands and subsequently leads to the formation of polar waves that propagate along the nematic band [Fig. 3(B), *SI Appendix*, Movies 1-3]. Initialising the system with different randomly disordered states, we find that this local polar instability leads to various distinct types of spatio-temporal dynamics including polar waves within nematic bands [Fig. 3(B), *SI Appendix*, Movie 1], complete replacement of nematic bands by polar waves (*SI Appendix*), Movie 2) and dynamic switching between nematic bands and polar waves (*SI Appendix*, Movie 3).

In summary, for low and high polar bias our kinetic Boltzmann approach is consistent with the classical conception of self-propelled particle systems with predominantly nematic or polar symmetry (4) including the formation of nematic band patterns and traveling polar waves at the onset of nematic and polar order, respectively. For moderate polar bias, stability analysis uncovers an additional transition from nematic solutions to polar solutions at a density $\rho^c_{\text{nem-pol}} > \rho^c_2$. This transition gives rise to novel spatio-temporal dynamics that are not predicted by linear stability analysis: Our numerical simulations reveal that the high density core of nematic bands can locally cross the threshold density $\rho^c_{\text{nem-pol}}$, which favors the formation of polar waves. This instability eventually results in traveling-wave solutions, as well as more complex dynamics such as coexisting polar waves and nematic bands, and dynamic rearrangements of nematic bands. Importantly, this implies that the symmetry of the emerging patterns critically depends on the dynamics of the system and is not already determined or apparent from the assumed alignment symmetry nor indicated by linear stability analysis. This shows that the symmetry of the spatio-temporal pattern is itself an emergent property, whose dynamics is based on a mutual feedback between pattern formation and *local* symmetry breaking due to the redistribution (accumulation) of mass (particle density).

**Simple hydrodynamic equations account for coexisting symmetries.** The kinetic Boltzmann equation serves as a useful starting point for the derivation of hydrodynamic theories for the dynamics close to the onset of order (25). These field theories, which are more amenable to theoretical analysis than the kinetic Boltzmann equation, have been successfully employed to reproduce and understand the observed phenomenology of active matter systems close to ordering transitions (4, 30).

In order to derive a closed set of hydrodynamic equations from the kinetic Boltzmann equation Eq. (3), previous studies (25) assumed that, close to the onset of polar or nematic order, the respective order fields $f_1$ and $f_2$ and their temporal and spatial variations, are small. This assumption yields scaling relations for $f_k$ which suggest systematic truncation schemes for the infinite sum in Eq. (3) to arrive at closed equations for the dominant hydrodynamic fields. Balancing terms in the Boltzmann equation, Peshkov et al. (13) have proposed the following scaling relations for a system of polar particles with a fully nematic collision rule ($\psi = 0$): $\rho - \bar{\rho} \sim \varepsilon$, $\{f_{2k-1}, f_{2k}\}_{k \geq 1} \sim \varepsilon^k$, $\partial_t \sim \varepsilon$ and $\partial_{x/y} \sim \varepsilon$. With these scaling relations, one can expand the sum in Eq. (3) retaining only terms up to order $\varepsilon^3$ to get closed equations for the order fields $f_{\{1,2,3,4\}}$. The equations for $f_3$ and $f_4$ yield expressions for $f_3$ and $f_4$ in terms of $f_1$ and $f_2$. In addition to the continuity equation for $f_0$, one arrives at the following hydrodynamic equations for $f_1$ and $f_2$:

$$\partial_t f_1 = -(\alpha_0 + \rho\alpha_1)f_1 + \alpha_2 f_1^* f_2 - \alpha_3 |f_2|^2 f_1$$
$$- \frac{1}{2}(\nabla\rho + \nabla^* f_2) + \gamma_1 f_2^* \nabla f_2, \tag{4a}$$

$$\partial_t f_2 = (-\beta_0 + \rho\beta_1)f_2 + \beta_2 f_1^2 - \beta_3 |f_2|^2 f_2 - \beta_3' |f_1|^2 f_2$$
$$- \frac{1}{2}\nabla f_1 + \gamma_2 \nabla\nabla^* f_2 - \gamma_3 f_1^* \nabla f_2 - \gamma_4 \nabla^*(f_1 f_2), \tag{4b}$$

which are related to the polar and nematic order parameter through Eq. (2). To simplify the notation, we defined $\nabla := \partial_x + \mathrm{i}\partial_y$ and the asterisks denote complex conjugation. The coefficients contain contributions from angular diffusion and combinations of the collision integrals $\mathcal{I}_{n,k}$ introduced in Eq. (3) (for explicit expressions see *SI Appendix*, Note 3). The first terms in Eq. (4a) and Eq. (4b), which are linear in the modes $f_1$ and $f_2$, suggest that nematic and polar order grow beyond the densities given by $\rho^c_2 = \beta_0/\beta_1$ and $\rho^c_1 = -\alpha_0/\alpha_1$, respectively (these expressions for $\rho^c_1$ and $\rho^c_2$ are in fact equivalent to the expressions discussed above in the linear stability analysis of Eq. (3)). In addition, even for densities below $\rho^c_1$, i.e. $(\alpha_0 + \alpha_1\rho) < 0$, the second term in Eq. (4a) might still lead to growth of polar order when $|f_2|$ is large enough and the second term in Eq. (4a) dominates the first.

Given the validity of Eq. (4) for systems with a fully nematic collision rule (13), one could hope that Eq. (4) provides a suitable hydrodynamic description in the presence of a (at least small) polar bias. However, when we extend the collision integrals $\mathcal{I}_{n,k}$ and thereby the coefficients in Eq. (4) towards a polar bias as depicted in 1(B),(C) and calculate the uniform solutions of Eq. (4) as well as their linear stability, we find that the resulting phase diagram of Eq. (4) [see *SI*

*Appendix*, Note 3, Fig.S3] critically differs from the phase diagram of Eq. (1) [Fig. 2(A)]. Most importantly, Eq. (4) does not feature a secondary transition from nematically ordered solutions to polar-ordered solutions for moderate polar bias as observed in Fig. 2(A) (dashed line). The discrepancy between the phase diagrams obtained from the solutions of Eq. (4) and Eq. (3) suggests that in the presence of a polar bias, modes $f_k$ with $|k| > 4$, which were neglected in the derivation of Eq. (4), become important. To test the relevance of modes with $|k| > 4$ we performed numeric simulations of the dynamics of the Fourier modes, Eq. (3), taking into account modes $f_k$ with $|k|$ up to a certain $k_h$ and setting all modes with $|k| > k_h$ and their derivatives to zero (for the numerical solution we used XMDS2 (31), a fast Fourier transform (FFT)-based spectral solver). Consistent with our simulations in real space [Fig.3(A)] we find stable nematic bands, nematic bands with polar instabilities, and polar traveling waves for small, moderate, and large polar bias, respectively. However, soon after the polar instabilities within nematic bands have triggered polar waves [see Fig.3(C)] our simulations show that the ensuing polar order diverges. This divergence in the numerical solution of Eq. (3) occurs even for relatively large cutoff mode numbers $k_h \gtrsim 12$ [*SI Appendix*, Note.3A, Fig.S4]. Taken together, these findings suggest that a crude truncation of Eq. (3), and, in particular, the reduced set of equations for the lowest two modes Eq. (4) with the coefficients determined by a scaling analysis of the kinetic Boltzmann equation, do not (fully) capture the dynamic transition of patterns as observed in Fig. 3.

Alternative coarse-grained approaches to active matter have constructed hydrodynamic equations mainly on the basis of symmetry arguments and small amplitude expansions in the order fields and their gradients (1, 2, 32). Those approaches study the phenomenology of the hydrodynamic equations as a function of the coupling coefficients, which are considered to be free phenomenological parameters. In the following, we take a *semi-phenomenological* approach which retains the functional dependencies of Eq. (4) arrived at by using the Boltzmann equation while exploring the phenomenology of this field theory for general coupling parameters. In the spirit of a generalized Ginzburg-Landau approach, we require that the now phenomenological parameters $\beta_0$ and $\beta_1$ are positive in order to reproduce a bifurcation from a disordered state to a nematic state at a critical density $\rho_2^c = \beta_0/\beta_1$. Likewise, to suppress a direct bifurcation from disorder to polar order, $\alpha_0$ and $\alpha_1$ are chosen to be positive as well. Under these conditions, uniform polar order only grows when the second term in Eq. (4a) is large enough. To ensure saturation for $f_1$ and $f_2$, the coefficients for the highest order terms, i.e. $\alpha_3$, $\beta_3$, and $\beta_3'$, are chosen to be positive. We argue that an increasing polar bias, which mingles polar and nematic collisions, leads to an enhanced coupling strength between fields of nematic symmetry (i.e. $f_{2k}, k \geq 1$) and polar symmetry (i.e. $f_{2k-1}, k \geq 1$). In Eq. (4a), this *polar-nematic coupling strength* is set by $\alpha_2$. To systematically study the effect of a varying polar-nematic coupling strength $\alpha_2$, we fixed all coefficients in Eq. (4) except for $\alpha_2$. For specificity,
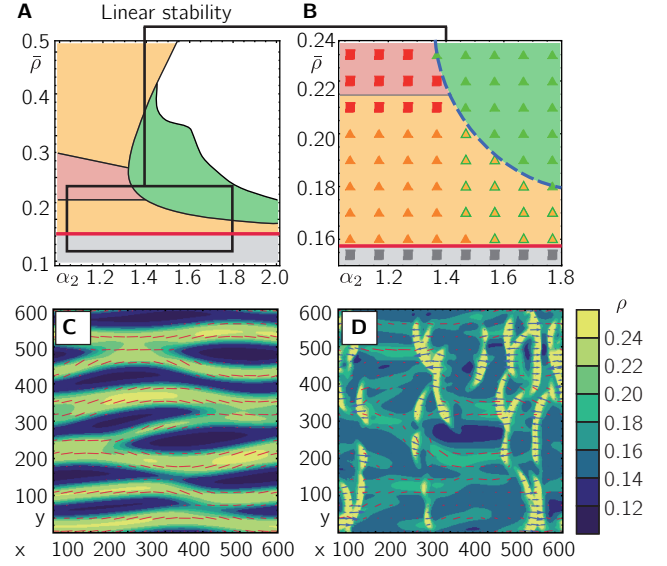


**Fig. 4. Cycling symmetries in hydrodynamic approach. (A)** Linear stability analyses of Eq. (4) yields a phase diagram with regimes of polar and nematic patterns that qualitatively resembles the phase diagram derived from the original kinetic Boltzmann approach for a mixed collision rule [Fig. 2; colors denote regimes of different symmetries and patterns as in Fig. 2(A) and 3(A)]. **(B)** Simulations [denoted by symbols, as in Fig. 3(A)] show the formation of nematic bands and polar waves, as well as coexistence patterns with transformations between nematic and polar patterns. **(C)** Snapshot of nematic band patterns shortly before the onset of local polar instabilities (red bars indicate orientation and strength of local nematic order). **(D)** At later times, polar instabilities lead to the formation of traveling wave patterns with complex dynamics including coexistence of local nematic and polar ordered regions which interact and transform into each other. Blue arrows denote the strength and direction of polar order. (Parameters are $\alpha_2 = 1.5$, $\bar{\rho} = 0.18$.). For details on the simulations see *SI Appendix*, Note 3B

all other coefficients were fixed to values derived from the kinetic Boltzmann equation with fully nematic alignment and slightly above the transition to nematic order ($\rho = \bar{\rho} = 0.16$ and $\sigma = 0.2$). This choice naturally satisfies all the above-mentioned general conditions on the coefficients.

By calculating the spatially uniform solutions of Eq. (4) and their linear stability against uniform and nonuniform perturbations, we obtain the phase diagram as a function of the average density $\bar{\rho}$ and the polar-nematic coupling strength $\alpha_2$ [see Fig. 4(A)]. This phase diagram shares key qualitative similarities with our linear stability analysis of the kinetic Boltzmann equation [Fig. 2(A)]. By construction, for average densities above $\rho_2^c$ the disordered solution is unstable and we find uniform solutions with nematic order [orange and red areas in Fig. 4(A)]. Slightly above $\rho_2^c$, these solutions are stable against uniform perturbations, but unstable against nonuniform perturbations perpendicular to the orientation of nematic order, suggesting the formation of nematic band patterns [orange area in Fig. 4(A)]. For moderate coupling strengths $\alpha_2$ ($\alpha_2 \gtrsim 1.4$ in units [density/time]), our linear stability analysis suggests a direct transition at $\rho_{\text{nem-pol}}^{(c,h)}$ from a phase of nematic band patterns to a phase of polar patterns [dotted line in Fig. 4(A)], similar to that observed in our analysis of the kinetic Boltzmann equation [dashed line in Fig. 2(A)]. When both $\alpha_2$ and $\bar{\rho}$ are large, there are no physical solutions (the polar order lies beyond the attainable density), indicating that our hydrodynamics equations are not

adequate in these regimes. At small $\alpha_2$ and large $\bar{\rho}$ we find re-entrance into a regime of nematic patterns. In the following we will disregard these regimes and focus on the regime close to the transition density $\rho_2^c$ [see highlighted regime in Fig. 4(A)].

To resolve the spatio-temporal dynamics of the modes $f_1$ and $f_2$ beyond linear stability analyses, we numerically solved equations Eq. (4), together with the continuity equation, using XMDS2 software. For low $\alpha_2 \lesssim 1.3$ and slightly above $\rho_c^2$, we find nematic band patterns as predicted by our linear analysis. For larger $\alpha_2$ and densities between $\rho_2^c$ and $\rho_{\text{nem-pol}}^{(c,h)}$, the system shows dynamic transitions between patterns of polar and nematic symmetry [see Fig. 4(B); *SI Appendix*, Movie 4] reminiscent of the observations in our kinetic Boltzmann approach [Fig. 3](B). First, the system forms nematic bands as predicted by linear stability analysis [Fig. 4(A)]. At the core of these bands the local density exceeds $\rho_{\text{nem-pol}}^{(c,h)}$, suggesting a local instability towards polar order (*SI Appendix*, Note 3B, Fig.S5). Accordingly, we observe the formation of travelling wave patterns along the nematic bands. These instabilities eventually result in intriguing spatio-temporal patterns of nematic and polar order which dynamically interconvert in a cyclic fashion [Fig. 4(C); *SI Appendix*, Note 3B, Movie 4].

## Discussion

Motivated by the intriguing dynamic coexistence of polar and nematic patterns observed in recent active matter experiments and simulations (17), we studied a system of self-propelled particles that exhibit binary nematic alignment interactions with a tunable polar contribution. For a moderate polar bias, our kinetic Boltzmann approach reveals a direct transition from a phase of macroscopic nematic to polar order for high enough densities. In addition to the previously studied nematic bands and traveling waves for respectively small and large polar bias (4, 25), we identify a parameter regime of moderate polar bias and density where a density increase in nematic patterns can induce a local symmetry-breaking instability and an ensuing transition to polar patterns. Depending on system size and initial conditions, this dynamic transition can lead to different final patterns, including coexistence of patterns with nematic and polar symmetry as well as dynamic transformations between them. We find a similar phenomenology in hydrodynamic equations when the coupling between polar and nematic order is strong enough.

Our findings shed new light on traditional symmetry assumptions in dilute active-matter theories (4) and suggest that the symmetry of patterns can depend on the (nonlinear) dynamics of the system. In the system we studied, a *global* symmetry-breaking instability of the uniform nematic state first leads to a redistribution of the density into nematic band patterns. Since in our system the density acts as control (bifurcation) parameter for the macroscopic symmetry, the high-density core of a nematic band can locally cross a threshold value in the density such that there is symmetry breaking, i.e. the symmetry of the system changes from nematic to polar. These *local* symmetry-breaking transitions eventually lead to

the self-organized coexistence of, and cycling between polar and nematic patterns. In contrast to coexistence of spatially distant patterns (5), here nematic and polar patterns are thus firmly intertwined: nematic bands serve as scaffolds for the creation of polar wave patterns, which propagate along the nematic bands and decay in its low-density neighborhood, which again fuels the formation of nematic bands. All of these observations are in very good agreement with the phenomenology observed in previous actomyosin motility assays and agent-based simulations of rods (17).

Previous studies have observed instabilities of nematic band structures in systems with fully nematic alignment interactions between polar particles (19, 33), particles with velocity reversal (34) and apolar particles (35, 36). There, for large enough system sizes, nematic bands exhibit a *transverse* instability, which causes long undulations and transverse break-up of nematic bands and can lead to chaotic dynamics (19, 33, 35, 36). While our large-scale simulations of the hydrodynamics equations also exhibit undulations of nematic bands [Fig. 4(B,C); *SI Appendix*, Movie 4], our system with mixed alignment symmetry features an additional instability of nematic bands towards polar order *parallel* to nematic bands, which leads to the formation of polar waves along the bands.

Our study highlights a *mutual feedback* between pattern formation and local symmetry-breaking instabilities (bifurcations) as the cause of dynamic coexistence between patterns of different symmetry. In a different but related context, the role of local equilibria and their stability has been studied for mass-conserving reaction-diffusion systems (37, 38). We hypothesize that this feedback is not limited to our study, but could be a more general principle whenever a control parameter (such as density) is dynamically redistributed during pattern formation. From a broader perspective on biological active matter, this could apply whenever individuals dynamically change their microscopic properties (velocity, interaction behavior, etc.) in response to macroscopic parameters such as the density. Prominent examples of such feedback between macroscopic effects and the microscopic components of the system are found synthetic active systems with chemical interactions (15), collective sensing in bacteria (39–41), and animals (14).

## Bibliography

1. Sriram Ramaswamy. The Mechanics and Statistics of Active Matter. *Annual Review of Condensed Matter Physics*, 1(1):323–345, aug 2010. ISSN 1947-5454. doi: 10.1146/annurev-conmatphys-070909-104101.

2. M Cristina Marchetti, Jean-François Joanny, Sriram Ramaswamy, Tanniemola B Liverpool, Jacques Prost, Madan Rao, and R Aditi Simha. Hydrodynamics of soft active matter. *Reviews of Modern Physics*, 85(3):1143, 2013.

3. Tamás Vicsek and Anna Zafeiris. Collective motion. *Physics Reports*, 517(3-4):71–140, 2012. ISSN 03701573. doi: 10.1016/j.physrep.2012.03.004.

4. Hugues Chaté. Dry Aligning Dilute Active Matter. *Annual Review of Condensed Matter Physics*, 11(1), 2020. ISSN 1947-5454. doi: 10.1146/annurev-conmatphys-031119-050752.

5. Markus Bär, Robert Großmann, Sebastian Heidenreich, and Fernando Peruani. Self-propelled rods: Insights and perspectives for active matter. *Annual Review of Condensed Matter Physics*, 11(1):441–466, 2020. doi: 10.1146/annurev-conmatphys-031119-050611.

6. Tamás Vicsek, András Czirók, Eshel Ben-Jacob, Inon Cohen, and Ofer Shochet. Novel Type of Phase Transition in a System of Self-Driven Particles. *Physical Review Letters*, 75(6):1226–1229, aug 1995. ISSN 0031-9007. doi: 10.1103/PhysRevLett.75.1226.

7. Guillaume Grégoire and Hugues Chaté. Onset of collective and cohesive motion. *Phys. Rev. Lett.*, 92:025702, Jan 2004. doi: 10.1103/PhysRevLett.92.025702.

8. Hugues Chaté, Francesco Ginelli, and Franck Raynaud. Collective motion of self-propelled

particles interacting without cohesion. *Physical Review E*, 77(4):046113, apr 2008. ISSN 1539-3755. doi: 10.1103/PhysRevE.77.046113.

9. Eric Bertin, Michel Droz, and Guillaume Grégoire. Boltzmann and hydrodynamic description for self-propelled particles. *Phys. Rev. E*, 74:022101, Aug 2006. doi: 10.1103/PhysRevE.74.022101.

10. Eric Bertin, Michel Droz, and Guillaume Grégoire. Hydrodynamic equations for self-propelled particles: Microscopic derivation and stability analysis. *Journal of Physics A: Mathematical and Theoretical*, 42(44), 2009. ISSN 17518121. doi: 10.1088/1751-8113/42/44/445001.

11. Hugues Chaté, Francesco Ginelli, and Raúl Montagne. Simple Model for Active Nematics: Quasi-Long-Range Order and Giant Fluctuations. *Physical Review Letters*, 96(18):180602, may 2006. ISSN 0031-9007. doi: 10.1103/PhysRevLett.96.180602.

12. Francesco Ginelli, Fernando Peruani, Markus Bär, and Hugues Chaté. Large-scale collective properties of self-propelled rods. *Physical Review Letters*, 104(18):184502, may 2010. ISSN 00319007. doi: 10.1103/PhysRevLett.104.184502.

13. Anton Peshkov, Igor S Aranson, Eric Bertin, Hugues Chaté, and Francesco Ginelli. Nonlinear field equations for aligning self-propelled rods. *Physical Review Letters*, 109(26):268701, 2012.

14. Andrew M Berdahl, Albert B Kao, Andrea Flack, Peter A H Westley, Edward A Codling, Iain D Couzin, Anthony I Dell, and Dora Biro. Collective animal navigation and migratory culture: from theoretical models to empirical evidence. *Philosophical Transactions of the Royal Society of London. Series B, Biological Sciences*, 373(1746):20170009, may 2018. ISSN 1471-2970. doi: 10.1098/rstb.2017.0009.

15. Olivier Dauchot and Hartmut Löwen. Chemical physics of active matter. *Journal of Chemical Physics*, 151(11):114901, 2019. doi: 10.1063/1.5125902.

16. Daniel Needleman and Zvonimir Dogic. Active matter at the interface between materials science and cell biology. *Nature Reviews Materials*, 2:17048 EP –, Jul 2017.

17. L Huber, R Suzuki, T Krüger, E Frey, and AR Bausch. Emergence of coexisting ordered states in active matter systems. *Science*, 361(6399):255–258, 2018.

18. Masoud Abkenar, Kristian Marx, Thorsten Auth, and Gerhard Gompper. Collective behavior of penetrable self-propelled rods in two dimensions. *Phys. Rev. E*, 88:062314, Dec 2013. doi: 10.1103/PhysRevE.88.062314.

19. Henricus H. Wensink, Jörn Dunkel, Sebastian Heidenreich, Knut Drescher, Raymond E. Goldstein, Hartmut Löwen, and Julia M. Yeomans. Meso-scale turbulence in living fluids. *Proceedings of the National Academy of Sciences*, 109(36):14308–14313, 2012. ISSN 0027-8424. doi: 10.1073/pnas.1202032109.

20. Ken H. Nagai, Yutaka Sumino, Raul Montagne, Igor S. Aranson, and Hugues Chaté. Collective motion of self-propelled particles with memory. *Phys. Rev. Lett.*, 114:168001, Apr 2015. doi: 10.1103/PhysRevLett.114.168001.

21. Robert Großmann, Pawel Romanczuk, Markus Bär, and Lutz Schimansky-Geier. Pattern formation in active particle systems due to competing alignment interactions. *The European Physical Journal Special Topics*, 224(7):1325–1347, 2015.

22. Sandrine Ngo, Francesco Ginelli, and Hugues Chaté. Competing ferromagnetic and nematic alignment in self-propelled polar particles. *Physical Review E - Statistical, Nonlinear, and Soft Matter Physics*, 86(5):4–8, 2012. ISSN 15393755. doi: 10.1103/PhysRevE.86.050101.

23. Andreas M Menzel. Collective motion of binary self-propelled particle mixtures. *Physical Review E*, 85(2):021912, 2012.

24. J Elgeti, R G Winkler, and G Gompper. Physics of microswimmers—single particle motion and collective behavior: a review. *Reports on Progress in Physics*, 78(5):056601, apr 2015. doi: 10.1088/0034-4885/78/5/056601.

25. A. Peshkov, E. Bertin, F. Ginelli, and H. Chaté. Boltzmann-Ginzburg-Landau approach for continuous descriptions of generic Vicsek-like models. *European Physical Journal: Special Topics*, 223(7):1315–1344, 2014. ISSN 19516401. doi: 10.1140/epjst/e2014-02193-y.

26. Jonas Denk, Lorenz Huber, Emanuel Reithmann, and Erwin Frey. Active curved polymers form vortex patterns on membranes. *Physical Review Letters*, 116(17):178301, 2016.

27. Khanh-Dang Nguyen Thu Lam, Michael Schindler, and Olivier Dauchot. Self-propelled hard disks: implicit alignment and transition to collective motion. *New Journal of Physics*, 17(11):113056, nov 2015. doi: 10.1088/1367-2630/17/11/113056.

28. Khanh-Dang Nguyen Thu Lam, Michael Schindler, and Olivier Dauchot. Polar active liquids: a universal classification rooted in nonconservation of momentum. *Journal of Statistical Mechanics: Theory and Experiment*, 2015(10):P10017, oct 2015. doi: 10.1088/1742-5468/2015/10/p10017.

29. Florian Thüroff, Christoph A. Weber, and Erwin Frey. Numerical treatment of the boltzmann equation for self-propelled particle systems. *Phys. Rev. X*, 4:041030, Nov 2014. doi: 10.1103/PhysRevX.4.041030.

30. Sriram Ramaswamy. Active matter. *Journal of Statistical Mechanics: Theory and Experiment*, 2017(5):054002, may 2017. doi: 10.1088/1742-5468/aa6bc5.

31. Graham R. Dennis, Joseph J. Hope, and Mattias T. Johnsson. Xmds2: Fast, scalable simulation of coupled stochastic partial differential equations. *Computer Physics Communications*, 184(1):201 – 208, 2013. ISSN 0010-4655. doi: https://doi.org/10.1016/j.cpc.2012.08.016.

32. John Toner and Yuhai Tu. Long-range order in a two-dimensional dynamical XY model: How birds fly together. *Phys. Rev. Lett.*, 75:4326–4329, Dec 1995. doi: 10.1103/PhysRevLett.75.4326.

33. L Giomi, L Mahadevan, B Chakraborty, and M F Hagan. Banding, excitability and chaos in active nematic suspensions. *Nonlinearity*, 25(8):2245–2269, jul 2012. doi: 10.1088/0951-7715/25/8/2245.

34. Robert Großmann, Fernando Peruani, and Markus Bär. Mesoscale pattern formation of self-propelled rods with velocity reversal. *Phys. Rev. E*, 94:050602, Nov 2016. doi: 10.1103/PhysRevE.94.050602.

35. Sandrine Ngo, Anton Peshkov, Igor S. Aranson, Eric Bertin, Francesco Ginelli, and Hugues Chaté. Large-scale chaos and fluctuations in active nematics. *Phys. Rev. Lett.*, 113:038302, Jul 2014. doi: 10.1103/PhysRevLett.113.038302.

36. Li-bing Cai, Hugues Chaté, Yu-qiang Ma, and Xia-qing Shi. Dynamical subclasses of dry active nematics. *Phys. Rev. E*, 99:010601, Jan 2019. doi: 10.1103/PhysRevE.99.010601.

37. J Halatek and E Frey. Rethinking pattern formation in reaction–diffusion systems. *Nature Physics*, 14(5):507–514, 2018. ISSN 1745-2481. doi: 10.1038/s41567-017-0040-5.

38. Fridtjof Brauns, Jacob Halatek, and Erwin Frey. Phase-space geometry of reaction–diffusion dynamics. arxiv:1812.08684, 20 Dec 2018.

39. Brian K. Hammer and Bonnie L. Bassler. Quorum sensing controls biofilm formation in vibrio cholerae. *Molecular Microbiology*, 50(1):101–104, 2003. doi: 10.1046/j.1365-2958.2003.03688.x.

40. Markus Rein, Nike Heinß, Friederike Schmid, and Thomas Speck. Collective behavior of quorum-sensing run-and-tumble particles under confinement. *Phys. Rev. Lett.*, 116:058102, Feb 2016. doi: 10.1103/PhysRevLett.116.058102.

41. Brian A Camley. Collective gradient sensing and chemotaxis: modeling and recent developments. *Journal of Physics: Condensed Matter*, 30(22):223001, may 2018. doi: 10.1088/1361-648x/aabd9f.

42. Florian Thüroff, Christoph a. Weber, and Erwin Frey. Critical Assessment of the Boltzmann Approach to Active Systems. *Physical Review Letters*, 111(19):190601, nov 2013. ISSN 0031-9007. doi: 10.1103/PhysRevLett.111.190601.

43. Benoît Mahault. *Outstanding problems in the statistical physics of active matter*. PhD thesis, 2018.

## Supplementary Note 1: Kinetic Boltzmann equation

Following Refs. (9, 10), the kinetic Boltzmann equation for the orientational one-particle distribution function $f(\mathbf{r}, \theta, t)$ reads:

$$\partial_t f(\mathbf{r}, \theta, t) + v_0 \mathbf{e}(\theta) \cdot \partial_{\mathbf{r}} f(\mathbf{r}, \theta, t) = \mathcal{I}_{\text{diff}}[f] + \mathcal{I}_{\text{coll}}[f, f], \tag{5}$$

where $\mathcal{I}_{\text{diff}}$ and $\mathcal{I}_{\text{coll}}$ denote the diffusion and collision integrals, respectively. They are given by

$$\mathcal{I}_d[f] = -\lambda f(\theta) + \lambda \int_{-\pi}^{\pi} \mathrm{d}\theta' \int_{-\infty}^{\infty} \mathrm{d}\eta \; f(\theta') \, P_\sigma(\eta) \delta_{2\pi}(\theta' - \theta + \eta), \tag{6a}$$

$$\mathcal{I}_c[f] = -f(\theta) \int_{-\pi}^{\pi} \mathrm{d}\theta' \; \mathcal{R}(\theta, \theta') \, f(\theta') + \int_{-\pi}^{\pi} \mathrm{d}\theta_1 \; f(\theta_1) \int_{-\pi}^{\pi} \mathrm{d}\theta_2 \; \mathcal{R}(\theta_1, \theta_2) f(\theta_2) \int_{-\infty}^{\infty} \mathrm{d}\eta \; P_\sigma(\eta) \, \Psi_\eta(\theta_1, \theta_2, \theta). \tag{6b}$$

$P_\sigma(\eta)$ is a Gaussian distribution with standard variation $\sigma$ and $\delta_{2\pi}$ denotes a generalized Kronecker delta, imposing that the argument is zero modulo $2\pi$. $\mathcal{R}(\theta_1, \theta_2)$ denotes the differential cross section of two particles with orientations $\theta_1$ and $\theta_2$. For disc-like particles with diameter $d$, $\mathcal{R}(\theta_1, \theta_2)$ is given by $\mathcal{R}(\theta_1, \theta_2) = 4 v_0 d \sin(\frac{\theta_1 - \theta_2}{2})$ (9, 10). The binary interaction rule enters through the alignment function $\Psi_\eta(\theta_1, \theta_2, \theta)$:

For polar alignment: $\qquad \Psi_\eta(\theta_1, \theta_2, \theta) = \delta_{2\pi}\left(\frac{\theta_1 - \theta_2}{2} - \theta + \eta\right)$

For antipolar alignment: $\qquad \Psi_\eta(\theta_1, \theta_2, \theta) = \frac{1}{2}\delta_{2\pi}\left(\frac{\theta_1 - \theta_2}{2} - \theta + \frac{\pi}{2} + \eta\right) + \frac{1}{2}\delta_{2\pi}\left(\frac{\theta_1 - \theta_2}{2} - \theta - \frac{\pi}{2} + \eta\right)$

For an interaction rule with variable polar bias $\psi$ we assume polar alignment for an intermediate angle with $|(\theta_1 - \theta_2)| < \pi/2 + \psi$ and antipolar alignment otherwise. The parameter $\psi \in [0, \pi/2]$ thus characterizes the strength of the polar bias where for $\psi = 0$ and $\psi = \pi/2$ the collision rule reduces to fully nematic or polar collisions, respectively.

In the following, we rescale time, space, and density such that $v_0 = \lambda = d = 1$. Then, the only remaining free parameters are the noise amplitude $\sigma$, the polar bias $\psi$, and the mean particle density $\bar{\rho} = A^{-1} \int_A \mathrm{d}\mathbf{r} \int_{-\pi}^{\pi} \mathrm{d}\theta f(\mathbf{r}, \theta, t)$ measured in units of $\lambda/(dv_0)$, i.e., the number of particles found within the area traversed by a particle between successive diffusion events. In order to study solutions of the the kinetic Boltzmann equation Eq. (5), it is convenient to expand this equation for $f$ in terms of Fourier modes of the angular variable given by

$$f_k(\mathbf{r}, t) = \int_{-\pi}^{\pi} \mathrm{d}\theta \; \mathrm{e}^{\mathrm{i}\theta k} f(\mathbf{r}, \theta, t). \tag{7}$$

The dynamics $f_k(\mathbf{r}, t)$ is then given by

$$\partial_t f_k + \frac{v_0}{2}\left[\partial_x(f_{k+1} + f_{k-1}) - \mathrm{i}\partial_y(f_{k+1} - f_{k-1})\right] = -\lambda(1 - \mathrm{e}^{-(k\sigma^2)/2})f_k + \sum_{n=-\infty}^{\infty} \mathcal{I}_{n,k} f_n f_{k-n}, \tag{8}$$

where the Fourier transform of the collision integral, $\mathcal{I}_{n,k}$, has contributions coming from polar and antipolar alignments depending on the polar bias $\psi$:

$$\mathcal{I}_{n,k} = \underbrace{\int_{-\frac{\pi}{2} - \psi}^{\frac{\pi}{2} + \psi} \frac{\mathrm{d}\Delta}{2\pi} \mathcal{R}(|\Delta|)\left[P_\sigma \cos(\Delta(n - \frac{k}{2})) - \cos(\Delta n)\right]}_{\rightsquigarrow \text{polar alignment}} + \underbrace{\int_{\frac{\pi}{2} + \psi}^{2\pi - \frac{\pi}{2} - \psi} \frac{\mathrm{d}\Delta}{2\pi} \mathcal{R}(|\Delta|)\left[P_\sigma \cos(\frac{k\pi}{2})\cos(\Delta(n - \frac{k}{2})) - \cos(\Delta n)\right]}_{\rightsquigarrow \text{antipolar alignment}}. \tag{9}$$

In order to find approximate stationary, spatially uniform solutions $\{f_k^{(0)}\}$ of Eq. (8) we followed Ref. (26) and first calculated the uniform steady state solutions for $\{f_k^{(0)}\}$ with $k \leq k_c$ of Eq. (8) setting all angular Fourier modes with $k > k_h$ as well as all spatial and temporal derivatives to zero. Depending on the global density $\bar{\rho}$ and the polar bias $\psi$, we find disordered solutions ($f_k^{(0)} = 0, k = 1, ...k_c$), solutions with purely nematic order ($f_2 k^{(0)} > 0, f_2 k - 1^{(0)} = 0 \; k = 1, ...k_c$), and solutions with polar order ($f_2 k^{(0)} > 0, f_2 k - 1^{(0)} > 0 \; k = 1, ...k_c$).

Next, we studied the stability of the these solutions by substituting $\rho = \bar{\rho} + \delta\rho$ and $f_k = f_k^{(0)} + \delta f_k$ with wave-like perturbations of the form

$$\delta\rho(\mathbf{r}, t) \sim \delta\rho_{\mathbf{q}} \, e^{i\mathbf{q}\cdot\mathbf{r}}, \qquad \text{and} \qquad \delta f_k(\mathbf{r}, t) \sim \delta f_{k,\mathbf{q}} \, e^{i\mathbf{q}\cdot\mathbf{r}}, \tag{10}$$

where $\delta\rho_{\mathbf{q}}$ and $\delta f_{k,\mathbf{q}}$ are in general complex amplitudes that are assumed to be small. Periodic boundary conditions in our numeric solution impose $|\mathbf{q}| = n\frac{2\pi}{L}$, $n\epsilon\mathbb{Z}$, where $L = \sqrt{A}$ and $A$ is the area of the (quadratic) system. The linearized set of equations of motion for the perturbations $\delta\rho_{\mathbf{q}}(t)$, $\delta f_{k,\mathbf{q}}(t)$ and $\delta f_{k,\mathbf{q}}^*(t)$ then read

$$\partial_t \delta f_k = -\frac{v_0}{2}(\nabla\delta f_{k-1} + \nabla^*\delta f_{k+1}) + \lambda(\hat{P}_{0,k} - 1)\delta f_k + \sum_{n=-\infty}^{\infty}(\mathcal{I}_{n,k} + \mathcal{I}_{k-n,k})|f_{k-n}|\delta f_n. \tag{11}$$

Substituting Eq. (10) into Eq. Eq. (11), we solved the resulting linear set of equations for the maximal eigenvalue as a function of the wave vector $\mathbf{q}$. The real part of this eigenvalue sets the linear growth rate of the respective perturbation. A solution $\{f_k^{(0)}\}$ is linearly unstable when there is a perturbation with positive growth rate and stable otherwise. Specifically, we probed the stability of spatially uniform solutions against spatial perturbations parallel and perpendicular their order.

As summarized in Fig. 2(A), we find that for low densities, the only uniform solution is the disordered state and it is linearly stable. For larger densities we find spatially uniform solutions of purely nematic order or polar order that are stable against perturbations for arbitrary $\mathbf{q}$ (denoted respectively as uniform nematic and polar states in Fig. 2(A)). Moreover, we find regimes in which solutions with purely nematic order or polar order are stable against uniform perturbations, i.e. $|\mathbf{q}| = 0$, but not against spatial perturbations, i.e. $|\mathbf{q}| > 0$. For solutions with nematic order, the growth rate of perturbations in the respective regime is maximal when the perturbation is *perpendicular* to the nematic order, while for solutions with polar order, the growth rate of perturbations in the respective regimes is maximal when the perturbation is *parallel* to the polar order. This indicates the formation of nematic band patterns and polar wave pattern, respectively (as denoted in Fig. 2(A)). In another regime, denoted as 'bistability' in Fig. 2(A), we find a disordered solution, which is stable against arbitrary perturbations, and–at the same time–a solution with polar order, which is stable against uniform but unstable against non-uniform perturbations. This indicates the existence of both linearly stable disorder and polar wave patterns, depending on the initial conditions of the system. In Fig. 2(A),(B) we used $k_c = 10$, however, choosing larger $k_c$ only leads to negligible quantitative changes of the stability diagram Fig. 2(A) and the uniform solutions Fig. 2(B).

## Supplementary Note 2: Numeric simulations

In order to study the nonlinear dynamics and steady states in the kinetic Boltzmann equation in real space Eq. (5) we employed the SNAKE algorithm as introduced in Ref. (42). As tessellations we used a quadratic periodic regular lattice with periodic boundary conditions with equally sized angular slices varying from 40 to 80. To account for an alignment rule between the angular slices $\theta_i$ and $\theta_j$ with variable polar bias we assume polar alignment for an intermediate angle $|(\theta_i - \theta_j)| < \pi/2 + \psi$ and antipolar alignment otherwise. For Figs. 2(B,C), we used only one lattice point in order to obtain the spatially uniform solution, while for Fig. 3 we used a $60 \times 60$ lattice with lattice spacing 10. Hence, the simulated system size is $A = 600 \times 600$. The computation time step was set to 0.3. The system was initialized with a disordered state with small random density fluctuations around the mean density $\bar{\rho} = A^{-1}\int_A \rho(\mathbf{r}, t)$. For densities $\bar{\rho}$ close to the onset of order we find the formation of spatial patterns: in the regime where our linear stability analysis [Fig. 2(A)] predicts polar patterns we observe traveling wave patterns as reported in Refs. (42) for fully polar alignment [see Fig. S1(A)]. For vanishing and small polar bias and close to $\rho_2^c$ we see the formation of nematic band patterns [see Fig. S1(B)]. The regimes of patterns and uniformly ordered solutions are in good agreement with our linear stability analysis. Similar to previous comparisons between linear stability analysis and solutions based on the SNAKE algorithm(26), the regimes of patterns in our numerical simulations are more restricted in parameter space than predicted by linear stability analysis [Fig. 3(A)], probably due to numerical diffusion in the discrete implementation of the SNAKE algorithm (43).

As detailed in the main text, for intermediate polar bias and densities, we find initially forming nematic bands which undergo an instability of polar order and eventually transform into patterns of coexisting and cycling polar and nematic symmetry (see Movie 1). We argue that this instability occurs since the density in the high density core of the nematic band exceeds the transition density $\rho_{\text{nem-pol}}^c$, above which polar order grows exponentially. This is shown in Fig. S2, where we plot the local dynamics of the density, the polar and nematic order parameter within a nematic band and in the disordered area between two bands.

Depending on the system size and random seed of initial conditions, we observe that the polar instability within nematic bands can lead to different patterns with polar and nematic symmetry including replacement of nematic bands by polar waves [see Movie 2], coexistence of nematic bands and polar waves [see Movie 1] or alternating formation of nematic bands and polar waves [see Movie 3].

## Supplementary Note 3: Hydrodynamic equations

In order to derive closed hydrodynamic equations from the kinetic Boltzmann equation Eq. (5), we follow (25) and assume that close to the onset of polar or nematic order the respective fields $f_1$ and $f_2$ as well as temporal and spatial variations are small. This assumption suggests scaling relations which allow to truncate the infinite sum in Eq. (8) and get closed equations for the dominant hydrodynamic fields.

Balancing terms in the Boltzmann equation Peshkov et al. (13) have proposed scaling relations for a system of polar particles with fully nematic collisions (i.e. $\psi = 0$) according to

$$\rho - \hat{\rho} \sim \varepsilon, \{f_{2k-1}, f_{2k}\}_{k \geq 1} \sim \varepsilon^k, \partial_t \sim \varepsilon, \partial_{x/y} \sim \varepsilon. \tag{12}$$

With these scaling relations, one can expand the sum in Eq. (8) retaining only terms of order $\varepsilon^3$ to get closed equations for the order fields $f_{1,2,3,4}$. The equations for $f_3$ and $f_4$ yield expressions for $f_3$ and $f_4$ in terms of $f_1$ and $f_2$ and one arrives at the following hydrodynamic equations for $f_1$ and $f_2$:

$$\partial_t f_1 = -(\alpha_0 + \rho \alpha_1) f_1 + \alpha_2 f_1^* f_2 - \alpha_3 |f_2|^2 f_1 - \frac{1}{2}(\nabla \rho + \nabla^* f_2) + \gamma_1 f_2^* \nabla f_2, \tag{13a}$$

$$\partial_t f_2 = (-\beta_0 + \rho \beta_1) f_2 + \beta_2 f_1^2 - \beta_3 |f_2|^2 f_2 - \beta_3' |f_1|^2 f_2 - \frac{1}{2} \nabla f_1 + \gamma_2 \nabla \nabla^* f_2 - \gamma_3 f_1^* \nabla f_2 - \gamma_4 \nabla^* (f_1 f_2), \tag{13b}$$

where $\nabla := \partial_x + i \partial_y$ and the star denotes complex conjugation. The coefficients are given by

$$\alpha_0 = 1 - P_1(\sigma), \tag{14a}$$
$$\alpha_1 = -(\mathcal{I}_{0,1}(\sigma) + \mathcal{I}_{1,1}(\sigma)), \tag{14b}$$
$$\alpha_2 = (\mathcal{I}_{-1,1}(\sigma) + \mathcal{I}_{2,1}(\sigma)), \tag{14c}$$
$$\alpha_3 = -4\gamma_2 (\mathcal{I}_{-2,1}(\sigma) + \mathcal{I}_{3,1}(\sigma))(\mathcal{I}_{1,3}(\sigma) + \mathcal{I}_{2,3}(\sigma)) \tag{14d}$$
$$\beta_0 = 1 - P_2(\sigma), \tag{14e}$$
$$\beta_1 = (\mathcal{I}_{0,2}(\sigma) + \mathcal{I}_{2,2}(\sigma)) \tag{14f}$$
$$\beta_2 = \mathcal{I}_{1,2}(\sigma), \tag{14g}$$
$$\beta_3 = -4\gamma_2 \mathcal{I}_{2,4}(\sigma)(\mathcal{I}_{-2,2}(\sigma) + \mathcal{I}_{4,2}(\sigma)) \tag{14h}$$
$$\beta_3' = -4\gamma_2 (\mathcal{I}_{1,3}(\sigma) + \mathcal{I}_{2,3}(\sigma))(\mathcal{I}_{-1,2}(\sigma) + \mathcal{I}_{3,2}(\sigma)), \tag{14i}$$
$$\gamma_1 = -2\gamma_2 (\mathcal{I}_{3,1}(\sigma) + \mathcal{I}_{-2,1}(\sigma)), \tag{14j}$$
$$\gamma_2 = 1/(4(1 - P_3(\sigma) - (\mathcal{I}_{3,3}(\sigma) + \mathcal{I}_{0,3}(\sigma)))), \tag{14k}$$
$$\gamma_3 = 2\gamma_2 (\mathcal{I}_{-1,2}(\sigma) + \mathcal{I}_{3,2}(\sigma)), \tag{14l}$$
$$\gamma_4 = 2\gamma_2 (\mathcal{I}_{1,3}(\sigma) + \mathcal{I}_{2,3}(\sigma)), \tag{14m}$$

where $P_k(\sigma) = e^{-k^2 \sigma}$ and $\mathcal{I}_{n,k}(\sigma)$ are collision integrals defined in Eq. (9). For a fully nematic collision rule, the coefficients $\alpha_0, \alpha_1, \alpha_2, \alpha_3, \beta_0, \beta_1, \beta_2, \beta_3'$ are positive. As discussed in the main text, this defines a critical density $\bar{\rho} = \beta_0/\beta_1$ above which the disordered state is unstable against growth of nematic order, whereas polar order will always decay to linear order.

In principle, one could argue that these equations, which were derived for a fully nematic collision rule, might still be useful to study a system including a small polar bias. Indeed, the coefficient $\alpha_1$ becomes negative for larger polar bias defining a critical density at $\bar{\rho} = -\alpha_0/\alpha_1$ above which the disordered state is linearly unstable against growth of polar order. The transition densities for nematic order $\bar{\rho} = -\beta_0/\beta_1$ and polar order $\bar{\rho} = -a_0/a_1$ are in fact equivalent representations of the conditions $\mu_2(\bar{\rho}, \sigma, \psi) = 0$ and $\mu_1(\bar{\rho}, \sigma, \psi) = 0$, respectively, derived in the main text. We therefore included the dependence of the collision integrals on the polar bias $\psi$ as given by Eq. (9). Even for $(\alpha_0 + \alpha_1 \rho) < 0$ equation Eq. (13a) might allow a polar instability when the second term, which is linear in $f_2$, dominates the first term.

To test the validity of equations Eq. (13) in the presence of a polar bias we numerically calculated the phase diagram derived from Eq. (13) [see Fig. S3]. For specificity, we fixed noise value to $\sigma = 0.2$. Already for zero and small polar bias we find a transition from nematic to polar order for high densities. However, this is likely an artefact from the truncation procedure which is suited for densities close to the order transition. In this high density regime, numerical solutions of equations Eq. (13) for a nematic collision rule without polar bias show unbounded growth (13), indicating that higher orders neglected in the derivation of Eq. (13) become important (13). Apart from this unphysical transition to polar order for high densities at small polar bias the phase diagram of equations Eq. (13) also features a regime of polar order for larger polar bias bias. Here, similar as in Fig. 2, polar order is not restricted to densities above $\rho_1^c$ but is also present above the transition to nematic order marked by $\rho_2^c$. However, unlike the phase diagram for the kinetic Boltzmann equation [Fig. 2(A)], the phase diagram of the hydrodynamic equations Eq. (13), Fig. S3, lacks a pronounced transition from a purely nematic phase to a phase of polar order. Altogether, equations Eq. (13) with the coefficients Eq. (14) do not fully capture the phenomenology of a transition between nematic and polar patterns as observed in Fig. 2(A),(C).

**A. Simulations including higher angular Fourier modes.** The difference between the diagram in Fig. S3 and Fig. 2(A),(C) suggest, that to capture the transformations between nematic and polar patterns as observed in Section 2 higher orders that have been neglected in the derivation of Eq. (13) become important. To test this hypothesis, we simulate the Boltzmann equation in angular Fourier space Eq. (8) including the continuity equation for the density taking into account modes $f_k$ with $|k|$ up to a certain $k_h$ and setting all modes with $|k| > k_h$ and their derivatives to zero. Furthermore, we assumed periodic boundary conditions. For the numerical solution we used XMDS2 (31), a fast Fourier transform (FFT)-based spectral solver. In the parameter regime where our simulations in real space [see Ref. 2] show transformation between nematic bands and polar patterns, we find the formation of nematic bands which undergo a polar instability [see Fig. S4]. However, this polar instability leads to a divergence in the polar order parameter in our simulations. We obtain a similar result for numeric simulations of Eq. (8) with $k_h = 6$ as well as when we employ truncation assumptions other than the one detailed in the main text and Section 3 (e.g. when we close the truncation in 3 at $\epsilon^5$ instead of $\epsilon^3$).

**B. Generalized hydrodynamic equations.** For linear stability analysis and numeric simulations of the hydrodynamic equations Eq. (8) together with the continuity equation [shown in Fig.4A,B] we use the parameters values

$$\alpha_0 = 0.019801326693244747, \tag{15a}$$
$$\alpha_1 = 0.4496250137624467, \tag{15b}$$
$$\alpha_3 = 2.1897054378862726, \tag{15c}$$
$$\beta_0 = 0.07688365361336424, \tag{15d}$$
$$\beta_1 = 0.48867097895034317, \tag{15e}$$
$$\beta_3 = 3.007210976282877, \tag{15f}$$
$$\beta_2 = -0.12486399707430346, \tag{15g}$$
$$\beta_3' = -0.612545745821566, \tag{15h}$$
$$\gamma_1 = 0.5258429516101398, \tag{15i}$$
$$\gamma_2 = 0.44601012183492805, \tag{15j}$$
$$\gamma_3 = 0.14709871812254954, \tag{15k}$$
$$\gamma_4 = 1.857267053107399, \tag{15l}$$

where units have been suppressed but can be easily read of from Eq. (13). This corresponds to the values in Eq. (14) for $\sigma = 0.2$ and a density $\bar{\rho} = 0.16$ close above the critical density $\rho_2^c$. As discussed in the main text, we now vary the nematic-polar coupling strength $\alpha_2$ and $\bar{\rho}$. Using XMDS2 (31) and a system size of 200 on a $80 \times 80$ lattice, we scanned the parameter regime as indicated in Fig. 4(B) and found regimes of stable nematic band patterns, polar wave patterns, and transformations between nematic patterns due after local instabilities in the high density cores of nematic bands. Figure S5 shows the local density and nematic order which cross the critical nematic order above which polar order grows. In the parameter regime of transformations between nematic and polar patterns, for large system sizes we observe intriguing patterns of coexisting polar waves and nematic bands which closely interact and transform into each other in a cyclic fashion [Fig. 4(D), Movie 4], similarly as observed in Ref. (17).
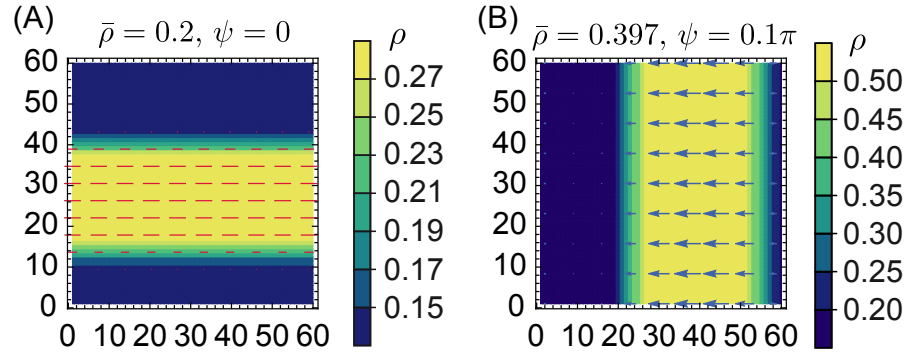
## Supplementary Note 4: Supplemental figures



**Fig. S1. Spatial patterns in simulations.** For different values of $\bar{\rho}$ and polar bias $\psi$, we find nematic bands (A) and polar traveling waves (B), in agreement with our linear stability analysis, Fig. 2(A). The color denotes the local density, red bars and blue arrows indicated the orientation and strength of local nematic and polar order, respectively. Simulations were done on a $60 \times 60$ lattice with a spacing $10$ and $80$ angular slices. The time step was set to $0.3$.
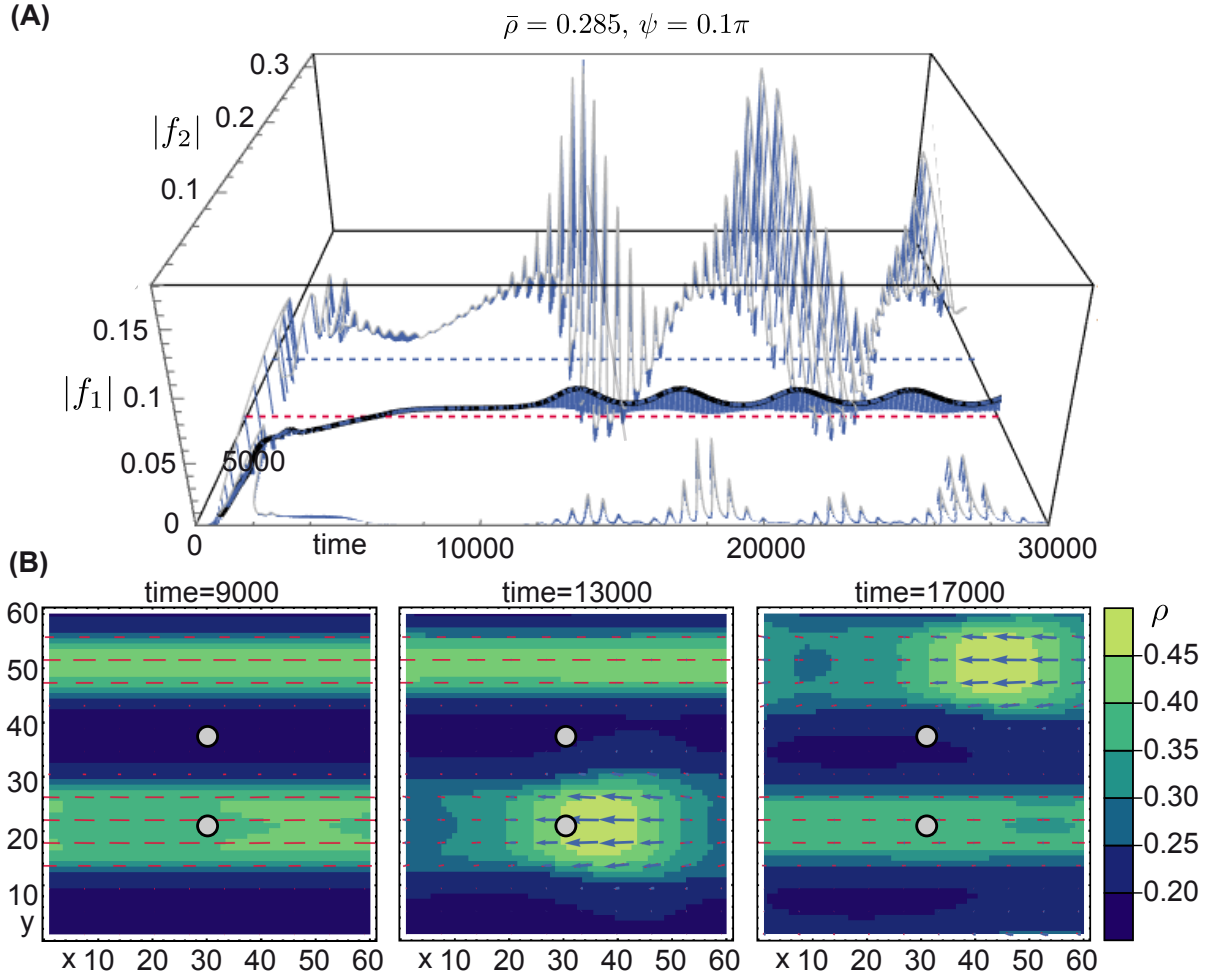
**Fig. S2. Polar instability in the kinetic Boltzmann approach. (A)** Time trace of nematic and polar order parameters (respectively $|f_2|$ and $|f_1|$) close to the core of a nematic band and in the disordered region of nematic band pattern (gray lines) as well as the average nematic and polar order (black line). Red and blue dashed lines denote the uniform steady state solution for the nematic order and the nematic order that corresponds to the critical density $\rho^c_{\text{nem-pol}}$, respectively. After the formation of a nematic band, the nematic order within the band exceeds the value corresponding to $\rho^c_{\text{nem-pol}}$ while in the disorder region the nematic order drops to zero. After some time polar order starts to grow within the band, which leads to the growth of global polar order. The distance between the time traces and the x-y-plane is marked by blue bars to emphasize the growth of polar order more clearly. **(B)** Snapshots at different time points before and after the polar instability shown in (A). For the respective movie, see Movie 1.
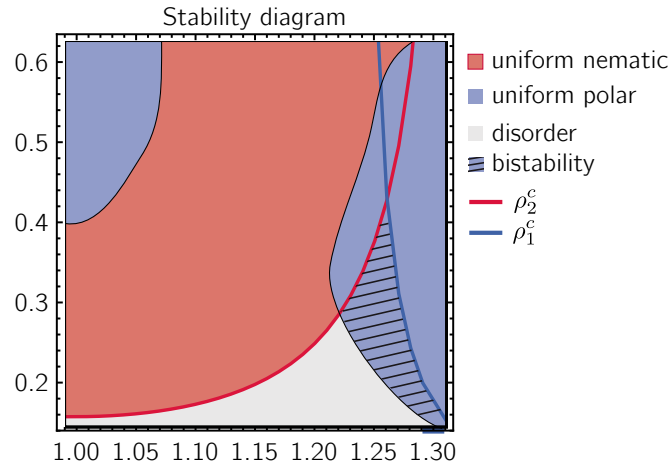
**Fig. S3. Stability diagram of kinetic Boltzmann-hydrodynamic equations with fully nematic truncation scheme.** The color shows different regimes in which solutions of disorder, nematic order and polar order are stable against uniform solution. Unlike the stability diagram Fig. 2(A), the phase diagram lacks a pronounced transition from nematic to polar steady states for moderate polar bias. In addition, there is an unphysical regime of polar order already for zero and small polar bias at large densities.
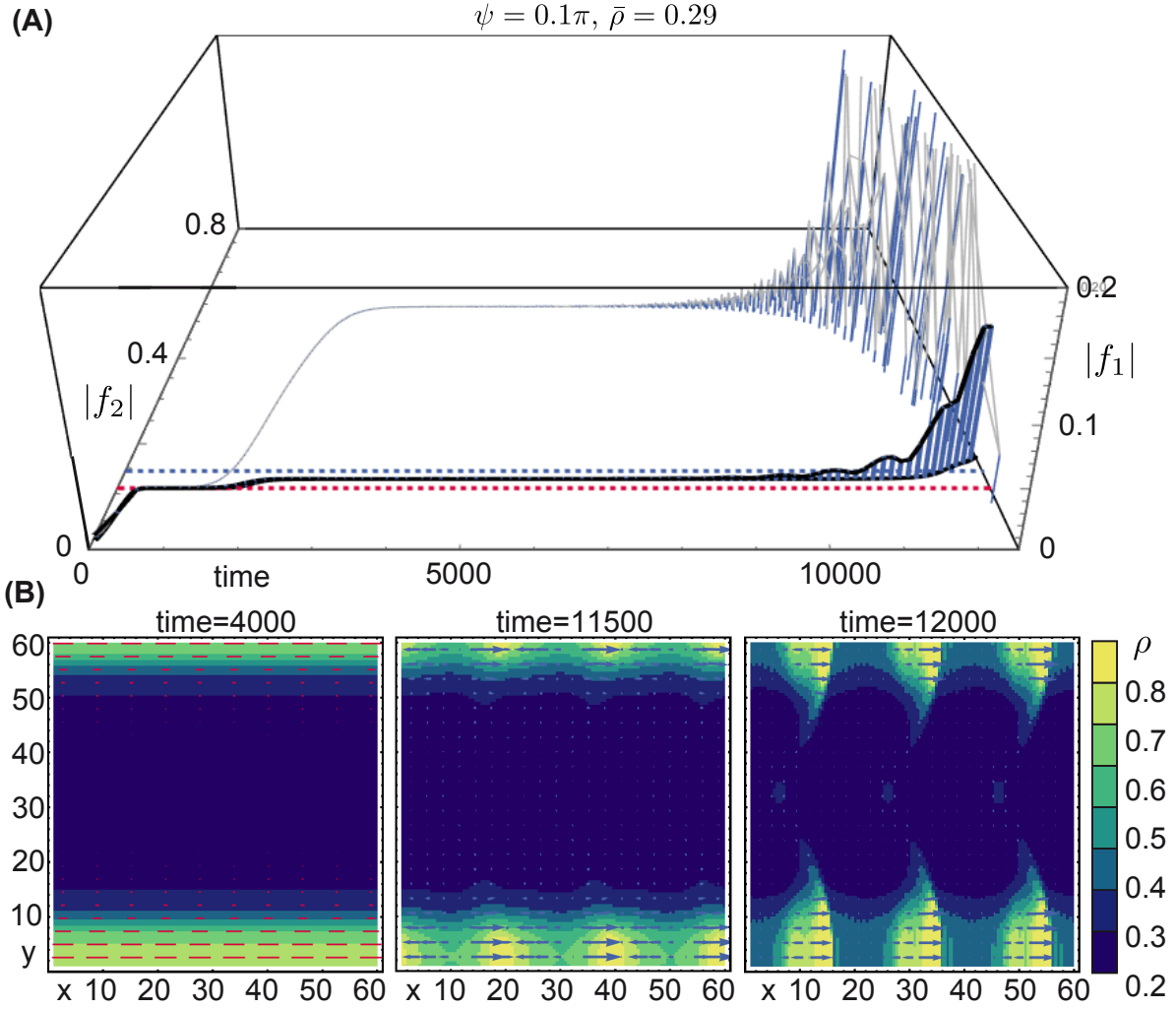
**Fig. S4. Polar instability in the kinetic Boltzmann equation in Fourier space.** **(A)** Evolution of the nematic and polar order of one position in the core of a nematic band (grey line) and of the spatial average (black line). The red dashed line indicates the uniform steady state solution and the blue dashed line indicates the nematic order that corresponds to the critical density $\rho_{\text{nem-pol}}^{(c,h)}$. The nematic order in the nematic band exceeds the value corresponding to $\rho_{\text{nem-pol}}^{(c,h)}$ before after some time polar order builds up. The average global polar order grows accordingly. The distance to the x-y-plane is highlighted by blue bars. Soon after the polar order grows the numeric solution diverges. **(B)** Snapshots of the patterns at different time points. The color denotes the local density. Red bars and blue arrows indicate the orientations and strengths of the local nematic and polar order, respectively. The solutions were obtained using XMDS software (31) and using a cutoff $k_h = 12$ as detailed in Section A.
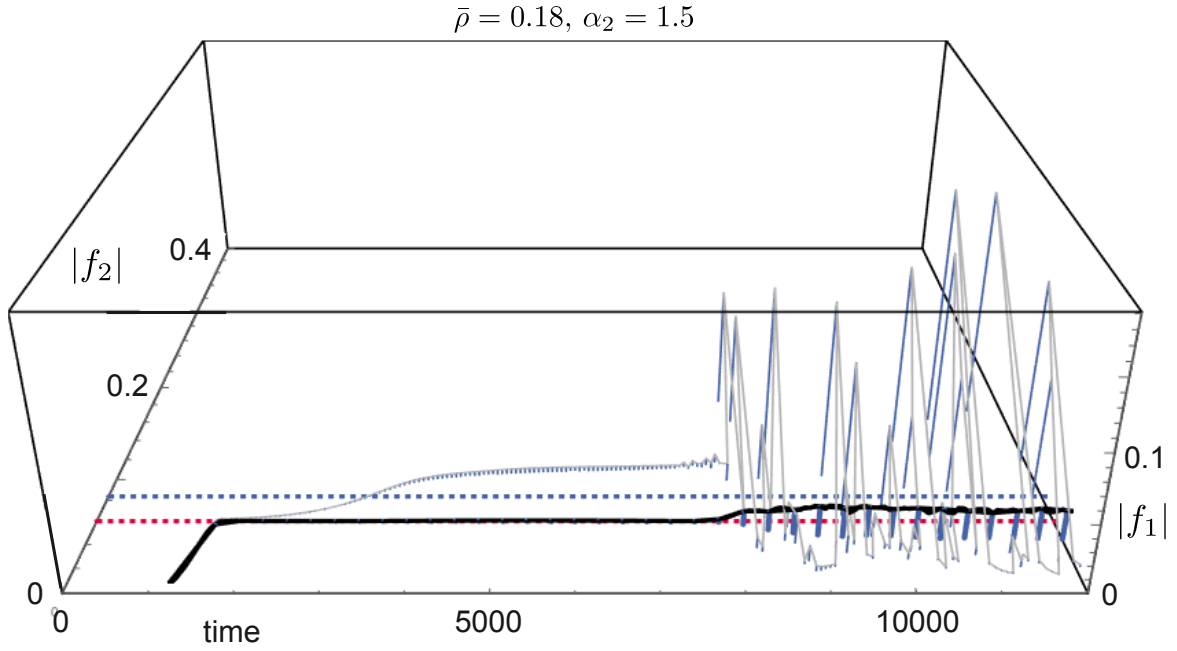
**Fig. S5. Polar instability in generalized hydrodynamic equations.** Evolution of the nematic and polar order of one position in the core of a nematic band (grey line) and of the spatial average (black line). The red dashed line indicates the uniform steady state solution and the blue dashed line indicates the nematic order that corresponds to the critical density $\rho_{\text{nem-pol}}^{(c,h)}$. The nematic order in the nematic band exceeds the value corresponding to $\rho_{\text{nem-pol}}^{(c,h)}$ before after some time polar order builds up. The average global polar order grows accordingly. The distance to the x-y-plane is highlighted by blue bars.

## Supplementary Note 5: Supplemental movie captions

For supplemental movies, please contact the authors.

**Movie 1: Transformations between nematic bands and polar waves.** Parameters are $\bar{\rho} = 0.292$ and $\psi = 0.1\pi$. Results were obtained based on a modified version of the SNAKE algorithm on a $100 \times 100$ lattice with spacing 8, time step 0.3 and 40 angular slices. The system started from isotropic disorder with small random fluctuations with a seed different to the seed in Movies 2 and 3. The color shows the local density according to the color bar and the axis denote the extensions in units of the lattice spacing.

**Movie 2: Nematic bands transform into polar waves.** Parameters are $\bar{\rho} = 0.285$ and $\psi = 0.1\pi$. Results were obtained based on a modified version of the SNAKE algorithm on a $100 \times 100$ lattice with spacing 8, time step 0.3 and 40 angular slices. Initial conditions were chosen uniform disordered with small random fluctuations with a seed different to the seed in Movies 1 and 3. The color shows the local density according to the color bar and the axis denote the extensions in units of the lattice spacing.

**Movie 3: Nematic bands transform into polar waves and back.** Parameters are $\bar{\rho} = 0.285$ and $\psi = 0.1\pi$. Results were obtained based on a modified version of the SNAKE algorithm on a $60 \times 60$ lattice with spacing 8, time step 0.3 and 40 angular slices. Initial conditions were chosen uniform disordered with small random fluctuations with a seed different to the seed in Movies 1 and 2. The color shows the local density according to the color bar and the axis denote the extensions in units of the lattice spacing.

**Movie 4: Coexistence and transformations of nematic bands and polar waves in generalized hydrodynamic equations.** Parameters are $\bar{\rho} = 0.17$, $\alpha_2 = 1.5$. The color denotes the local density as given in the colour bar. Simulation results were obtained with XMDS software(31) as detailed in A for a system of size $800 \times 800$ with 250 lattice points per dimension. The simulation was initiated from a uniform disordered state with small random perturbations and the movie starts after the initial formation of nematic bands. The color shows the local density according to the color bar and the axis denote the spatial extensions.